Original scientific paper

https://doi.org/10.33180/InfMIDEM2022.206

Informacije MIDEM

Journal of Microelectronics,
Electronic Components and Materials
Vol. 52, No. 2(2022), 129– 142

Analysis of effects of dangling-bond defects in doped a-Si:H layers in heterojunction silicon solar cells with different electron affinities of ITO contacts

Jošt Balent, Franc Smole, Marko Topič, Janez Krč

University of Ljubljana, Faculty of electrical engineering, Laboratory of Photovoltaics and Optoelectronics, Ljubljana, Slovenia

Abstract: The effects of dangling-bond defects in doped hydrogenated amorphous-silicon layers (p-a-Si:H and n-a-Si:H) in heterojunction silicon (SHJ) solar cells are studied in relation to applied Indium-Tin-Oxide (ITO) contacts with different electron affinities. A state-of-the-art numerical model of the SHJ solar cell was employed, including ITO contacts as full, volumetric semiconductor layers, applying the trap-assisted, band-to-band and direct tunnelling mechanisms at heterointerfaces in the device. The levels of dangling bond defect concentrations were varied in both p-a-Si:H and n-a-Si:H layers and ITOs with two different electron affinities were considered at both sides of the device. We show that the effects of the defects on the short-circuit current density, open-circuit voltage, fill factor and conversion efficiency of the device become more pronounced if ITOs with non-optimal electron affinities are used. Possibility to reach higher doping levels of the doped a-Si:H layers would mitigate the effects of its dangling bond states, which becomes more important if ITO electron affinity is not optimized to the doped a-Si:H layers. We demonstrate that the reduced efficiency due to the increase in dangling-bond density originates from the decrease of the fill-factor and open-circuit voltage, whereas the short-circuit current density has a small effect on efficiency for the chosen variation span. The reduction of the fill-factor is further explained by a drop in maximum-power-point voltage, which is more pronounced if optimization of ITO electron affinity is not taken into account.

Keywords: Silicon heterojunction solar cell; Opto-electrical simulation; Defect-states, Electron affinities

Numerična analiza učinkov defektov bingljajočih vezi v dopiranih plasteh iz a-Si:H v heterospojnih silicijevih sončnih celicah s kontakti ITO z različnimi elektronskimi afinitetami

Izvleček: Raziskali smo vpliv defektov bingljajočih vezi v dopiranih slojih hidrogeniziranega amorfnega silicija (p-a-Si:H in n-a-Si:H) v kombinaciji s kontakti iz indij-kositrovega oksida (ITO) pri heterospojnih silicijevih sončnih celicah (SHJ). Za raziskovanje notranjih in zunanjih lastnosti celice smo uporabili optoelektrične simulacije. Uporabljeni sodobni numerični model SHJ sončne celice je vseboval kontakte ITO, ki so bili modelirani kot dejanski polprevodniški sloji ter upošteval tuneliranje s pomočjo pasti, tuneliranje med energijskimi pasovi in tuneliranje znotraj energijskega pasu na heterospojih sončne celice. Spreminjali smo koncentracijo defektov bingljajočih vezi v p-a-Si:H in n-a-Si:H slojih pri dveh različnih elektronskih afinitetah kontaktov ITO na obeh straneh celice. Pokazali smo, da je vpliv defektov na izkoristek, polnilni faktor, napetost odprtih sponk in kratkostični tok bolj izražen, kadar elektronska afiniteta kontaktov ITO ni bila prilagojena dopiranim a-Si:H slojem. Ugotovili smo, da je zmanjšana učinkovitost zaradi povečanja gostote defektov bingljajočih vezi posledica zmanjšanja polnilnega faktorja in napetosti odprtih sponk, medtem ko kratkostični tok ni močno vplival na izkoristek znotraj izbranega območja variacije. Zmanjašanje polnilnega faktorja smo obrazložili preko upadanja napetosti pri maksimalni moči, ki se zmanjša še bolj občutno, kadar kontakti ITO niso optimizirani.

Ključne besede: heterospojne silicijeve sončne celice; optoelektrične simulacije; defektna stanja, elektronske afinitete

** Corresponding Author's e-mail: jost.balent@fe.uni-lj.si*

How to cite:
J. Balent et al., "Analysis of effects of dangling-bond defects in doped a-Si:H layers in heterojunction silicon solar cells with different electron affinities of ITO contacts", Inf. Midem-J. Microelectron. Electron. Compon. Mater., Vol. 52, No. 2(2022), pp. 129–142

1 Introduction

The ever-growing demand for clean and affordable electrical energy opened up a substantial market for photovoltaics and other renewable energy technologies. In Photovoltaics the biggest market share (~95 %) belongs to the crystalline-silicon (c-Si) based solar-cell technology [1]. Of these, silicon heterojunction (SHJ) solar cells are gaining attraction with the potential to achieve high conversion efficiency, low temperature coefficients and competitive production costs. The current world-record efficiency of a c-Si-based terrestrial non-concentrating large area solar cell is 26.7 % [2] and is achieved by the heterojunction structure in combination with interdigitated back contacting [3]. The SHJ cells utilize the benefits of both, conventional (c-Si wafer-based) and thin-film (hydrogenated amorphous silicon - a-Si:H) technologies. A thorough understanding of the governing physical mechanisms in state-of-the-art structures of solar cells, such as SHJ, is crucial when designing cells at the limit of what is theoretically possible (~30 % for single junction devices) [4]. Numerical modelling and simulations are an indispensable part of the R&D cycle as they unveil, often immeasurable, internal quantities of the solar cell, which determine its external characteristics. The study presented in this paper is based on detailed opto-electrical modelling and simulations of SHJ solar cells. In particular, we analyse the effects of dangling bond defects in doped a-Si:H layers in relation to indium tin oxide (ITO) transparent conductive oxide (TCO) contacts with different electron affinities χ. Various numerical models emerged from the research of SHJ cells that vary in complexity and accuracy [5]–[14]. In this contribution we used the Sentaurus TCAD software suite [15] to numerically model and study the device's internal and external performance related to the mentioned effects for applied ITO electrodes with optimized and non-optimal electron affinities. While our previous work [16] was focused on combined effects of defect states at i-a-Si:H/c-Si interfaces and in p-doped a-Si:H (p-a-Si:H) and n-doped (n-a-Si:H) thin layers considering one pre-selected electron affinity of ITO layers, in this work we extend the study to structures where ITO contacts have different electron affinities (optimized and non-optimal). Solar cells with ITO/doped a-Si:H selective contacts have already been studied numerically [11], [17]–[21] however, the authors either used a Schottky barrier as a Dirichlet boundary condition to model the ITO contacts or focused on other parameters of ITO and a-Si:H. Studies have not been performed in relation to specific defect types in a-Si:H doped layers in combination with different work functions or electron affinities of ITO contacts. In our research we use a fully volumetric semiconductor model of ITO, including the accompanying trap-assisted (TAT), band-to-band (BBT) and direct tunnelling (DT) processes in simulations. We focus our analysis primarily on the maximum-power-point (MPP) operation of the solar cell, as this is the common operating condition of solar cells in a real scenario and is often not taken in consideration sufficiently in such modelling studies. Quantitative results of the presented analysis reveal the impact of defects, in particular dangling-bond states in doped a-Si:H layers (especially in the p-a-Si:H layer) when using ITO contacts with different electron affinities. It is necessary to study also the synergy between the defect states and the ITO electron affinity as they both have a big influence on the electronic state of the device (formation of the electric field needed for charge separation), which determines the efficiency of the cell. Additionally, the study aims to improve the physical understanding of the related effects. Simulation results are presented for the a-Si:H based selective contacts, however, the results can be usefully considered also in the design of the SHJ solar cells including novel materials for selective contacts. e.g. metal-oxides and fluorides [8], [22]–[27].

2 Device structure and model

In our analysis we considered the following SHJ solar cell structure (Fig. 1): ITO front cathode (70 nm), p-doped a-Si:H layer (p-a-Si:H, 10 nm), intrinsic a-Si:H passivation layer at p-side (i-a-Si:H, 5 nm), n-doped c-Si bulk absorber (n-c-Si, 150 µm) with interface regions at both i-a-Si:H/n-c-Si interfaces (2 nm), intrinsic a-Si:H passivation layer at n-side (i-a-Si:H, 5 nm), n-doped a-

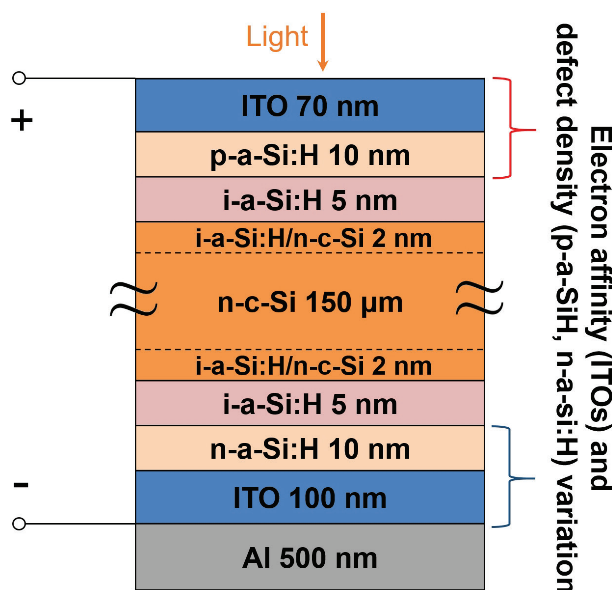

Figure 1: Structure of the simulated solar cell. Optical simulations were done on the entire device whereas electrical simulations used ideal ohmic boundary condition in lieu of the Aluminum layers.

Si:H layer (n-a-Si:H, 10 nm), rear anode ITO (100 nm)/ Al contact layer (500 nm). The ITO/p-a-Si:H and ITO/n-a-Si:H layer stacks enable selective collection of generated holes and electrons at the cathode and anode, respectively. The input parameters of layers and interface regions are described later.

The optical generation profile of the illuminated cell with standard AM1.5g spectrum was simulated with the Sun*Shine* simulator [28]. The coherent and incoherent nature of light was accounted for in the thick and thin layers, respectively, together with the light scattering and antireflection effects at the front and rear side of the device. Light enters into the device through the p-a-Si:H side (front) of the device in our basic case, however, selected simulation tests have been done also for the n-side illumination. In the simulated reference structure, the short-circuit current density (*J*sc), calculated directly from optical generations in the n-c-Si layer under AM1.5g solar spectrum, amounted to 39.06 mA/cm^2. The Optical generation profile was kept unchanged during sweeps of the investigated electrical parameters (peak dangling bond defect density and doping of p-a-Si:H and n-a-Si:H layers, ITO electron affinity) to selectively indicate their effect on the solar cell performance. It should be noted that in this study we did not focus on the optical performance of the device. We chose the presented planar architecture instead of an interdigitated back-contact (IBC) solution to minimize external influences, such as lateral currents, normally present in IBC devices, to more clearly show the effects of defect density and ITO electron affinity on SHJ solar cell performance. Detailed optical simulations can be found elsewhere [10, 29].

Detailed electrical simulations of the device were performed with the Sentaurus TCAD software suite [15], also used and validated for simulation of SHJ solar cell structures in previous publications [9], [10]. The material interfaces were generally considered as geometrically flat in electrical simulations. The simulation domain in electrical simulations of the device was two-dimensional, however, the problem at hand is one-dimensional. Therefore, the results of internal quantities were transformed in a one-dimensional function of the structure depth where applied. The temperature was kept at 300 K in all simulations. In the numerical description of the cell, the Drift-Diffusion model was employed to solve the Poisson equation coupled with the continuity equations for charge concentration inside the investigated solar cell structure. We used both Gummel and Newton solving schemes interchangeably to either ensure, or expedite the convergence of the simulations. The Fermi-Dirac statistics was used to accurately calculate free-charge density also in the regions of high effective dopant concentrations. Band-gap narrowing and mobility dependence on dopant density was not included in the analysis, which shortened the simulation time with negligible effect on results as tested before for selected cases. The recombination of charge in the n-c-Si bulk was based on the parametrization first implemented by Richter et. al. [30], which includes both Auger and Radiative recombination mechanisms and accurately calculates their impact on minority carrier life-times in a broad range of dopant concentrations and injection levels. The Shockley-Read-Hall (SRH) recombination in the n-c-Si bulk was modelled via life-time of minority carriers (10 ms). In a-Si:H layers the defect states were represented by donor-like (don) and acceptor-like (acc) tail and dangling-bond (db) states. The amphoteric nature of dangling bonds was taken into account by two Gaussian functions, describing the so called +/0 and 0/- charged states [31]. The donor-like tail and the +/0 dangling-bond states are positively charged when vacant and neutral when occupied by an electron. The acceptor-like tail and so-called 0/- dangling-bond states are neutral when vacant and negatively charged when occupied by an electron. The defect-density distribution of tail-states (N_{tail}) and dangling-bond states (N_{db}) along the band-gap of the p-a-Si:H layer for the reference cell is presented in Fig. 2.

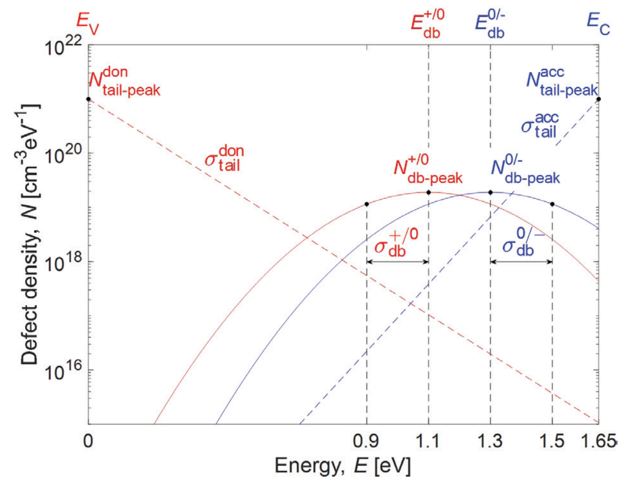

Figure 2: Representation of defect-state distribution in a-Si:H layers of the reference cell (selected case is shown for the p-a-Si:H layer, see corresponding values of the parameters for all a-Si:H based layers in Table I). The red dashed and full lines present the donor-like tail and +/0 dangling-bond states. The blue dashed and full lines correspond to acceptor-like tail and 0/- dangling-bond states.

However, all used defect-state parameters for the p-a-Si:H, n-a-Si:H, i-a-Si:H layers, and the i-a-Si:H/n-c-Si interface regions in the starting, reference cell are available in Table I. Regarding the defect-state variation, in this study we focused only on the values of the Gauss-

ian peak concentrations ($N^{+/0}_{db\text{-}peak}$, $N^{0/-}_{db\text{-}peak}$) and not the tail states, since it was indicated that they have a noticeable effect on device performance [16] including indium-tin-oxide (ITO). The defective n-c-Si surfaces (in simulations 2 nm regions) passivated by i-a-Si:H layers are described by dangling-bonds only, presented by two Gaussian peaks (see parameters in Table 1) and were also kept constant in this study. The ITO layers were modelled as semiconductor layers to fully encompass the band alignment with the a-Si:H layers, thus, taking into account the band-bending in both materials forming the heterojunction [17]. The electrical input parameters for ITO and all other layers are summarized in Table 2 in the Appendix.

Regarding the transport mechanisms at heterointerfaces, the transport through the i-a-Si:H/n-c-Si (encircled 1a and 2a in Fig. 3) heterojunctions is mediated by the inclusion of the built-in thermionic emission model [32], where for particle fluxes across the interface, the condition of continuous quasi-Fermi level and carrier temperature is used [33]. The thermionic emission at these interfaces is also supported by the trap-assisted tunnelling in our modelling approach [34], [35], which is also applied to the ITO/a-Si:H heterointerfaces (encircled 1 and 2 in Fig. 3).

The dominant tunnelling transport depends on the shape of the barrier [11], [21]. The transport through the ITO/p-a-Si:H barrier was modelled accordingly by the trap-assisted and band-to-band tunnelling, whereas at the ITO/n-a-Si:H interface by the trap-assisted and direct tunnelling. We used only non-local tunnelling models (variation of band energies and electric field over depth fully considered, guaranteed zero current at equilibrium). The use of non-local models is necessary since simpler, local models tend to underestimate the tunnelling current at low electric fields [37]. Direct (intra-band) and band-to-band tunnelling are considered as a sum of elastic (momentum of the particle is constant along the tunnelling path) and in-elastic or phonon-assisted (momentum changes across the tunnelling path) mechanisms and are based on [38] and [39]. Trap-assisted tunnelling is modelled similarly as a sum of elastic [34] and in-elastic processes [35].

In the reference cell the p-a-Si:H and n-a-Si:H layers doping densities were set to 2e19 cm^{-3} and 1.5e19 cm^3, corresponding to activation energies of 300 meV and 200 meV, respectively. Their electron affinity was set to 3.9 eV and their mobility-gaps to 1.65 eV and 1.72 eV, respectively. All other material and tunnelling parameters used for the reference case are presented in Table 2 in the Appendix.

Table 1: Defect-state parameters for a-Si:H layers and i-a-Si:H/n-c-Si interfaces

Quantity	Symbol	p-a-Si:H	n-a-Si:H	i-a-Si:H	i-a-Si/n-c-Si
Tails					
Tail peak concentrations	$N^{don}_{tailpeak}$ / $N^{acc}_{tail\text{-}peak}$ ($cm^{-3}eV^{-1}$)	1e+21 / 1e+21 [12]	1e+21 / 1e+21 [12]	1e+18 / 1e+18 [12]	/
Tail slopes	σ^{don}_{tail} / σ^{acc}_{tail} (meV)	120 / 70 [12]	60 / 40 [12]	120 / 70 [12]	/
Tail capture cross-sections (charged/neutral)	C^{ch}_{tail} / C^{n}_{tail} (cm^2)	1e-16 / 1e-16 [12]	1e-16 / 1e-16 [12]	7e-15 / 7e-17 [12]	/
Dangling bonds					
Dangling bonds peak Gaussian concentrations	$N^{+/0}_{dbpeak}$ / $N^{0/-}_{db\text{-}peak}$ ($cm^{-3}eV^{-1}$)	1.9e+19 / 1.9e+19 [12] *	2e+19 / 2e+19 [12] *	1e+16 / 1e+16 [12]	2.5e+17 / 2.5+e17 [36]
Dangling bonds std. deviations	$\sigma^{+/0}_{db}$ / $\sigma^{0/-}_{db}$ (meV)	200 / 200 [12]	200 / 200 [12]	150 / 150 [12]	200 / 200 [36]
Dangling bonds capture cross-sections (charged/neutral)	C^{ch}_{db} / C^{n}_{db} (cm^2)	5e-14 / 5e-15 [12] / [5]	5e-14 / 5e-15 [12]	2e-14 / 2e-15 [12]	1e-18 / 1e-19 [36]
Dangling bonds peak energies	$E^{+/0}_{db}$ / $E^{0/-}_{db}$ (eV)	1.1 / 1.3 [12]	0.45 / 0.7 [12]	0.9 / 1.1 [12]	0.46 / 0.66 [36]

* N_{dbpeak} values were changed from the reference in order to obtain realistic activation energies (300 meV and 200 meV) for the p-a-Si:H and n-a-Si:H layers, respectively.

3 Results and discussion

The goal of this analysis is to quantify and understand the effects related to different levels of defect states, in particular the dangling-bond Gaussian peaks ($N_{db\text{-}peak}$), in the p-a-Si:H and n-a-Si:H layers in a SHJ solar cell, for different affinities of ITO contacts as well as different doping levels of the a-Si:H layers.

We start the analysis with the energy band-diagrams of selected structures in thermal equilibrium (Fig. 3). The green, blue and red colours present the vacuum level, conduction and valence bands respectively. The fermi level is presented by the black line. Full lines depict the reference cell (parameters from Tables 1 and 2). Electron affinity of ITO at both sides is marked (double-arrows) for the reference case. The electron affinities of ITOs in the reference cell at the p- and n-sides ($\chi_{ITO\ p\text{-}side}$ = 5.30 eV and $\chi_{ITO\ n\text{-}side}$ = 4.56 eV) of the device have been selected according to [40], presenting realistic values close to the optimum case with respect to the low work function mismatch (ΔWF) between the ITOs and their adjacent doped a-Si:H layers (0.2 eV on both sides of the device) [19]. Please note that for our reference cell, to completely mitigate the mismatch of the work function just by manipulating the ITO electron affinity values, one would have to set them to 5.50 eV and 4.36 eV for the p-side and n-side, respectively. This could be achieved only for the ITO on the n-side of the device, since min. and max. values of electron affinities at the selected doping levels of ITO correspond to 4.2 eV and 5.3 eV [40]. However, besides ITO, there are also other TCO's that could be applied, namely Aluminum doped Zync-Oxide (AZO) and Antimony doped Tin-Oxide (ATO), as they both have high optical transparency due to high band gaps (> 3.1 eV) and can be doped sufficiently to provide a low resistance contact [40]. Regarding the range of possible work functions, AZO work functions range from 3.1 eV to 4.5 eV and for ATO the range is from 3.8 eV to 5.2 eV [40]. Out of these three, ITO offers the highest possible work function of 5.3 eV and is best suited for the ITO/p-a-Si:H contact stack. Other TCOs exhibit lesser optical or electrical parameters in comparison. A review of TCO material characteristics and their application to various solar cells is available in [40] and [41], respectively. The alternative, non-optimal values for the electron affinities of ITOs was the same on both sides ($\chi_{ITO\ p\text{-}side}$ = $\chi_{ITO\ n\text{-}side}$ = 4.93 eV) and resulted in a work-function mismatch of 0.57 eV (same for both sides). This type of symmetric mismatch allowed us to make a fair comparison between the two sides. During the analysis, we changed the electron affinity of ITO from its reference value to the non-optimal case on one side only, while maintaining the reference level on the other side. The dashed lines in Fig. 3 present the energy bands of the case, in which we varied the electron affinity of ITO only on the p-side, while the dash-dot-dot lines present the variation on the n-side. Since similar conditions, with respect to the energetic barriers at the heterointerfaces occur also in the MPP condition, we did not show it in this graph for the sake of simplicity. At the p-side, the two barriers related to the heterojunctions hinder the flow of holes generated in the n-c-Si absorber towards the front ITO, whereas on the n-side they impede the flow of electrons toward the rear ITO contact.

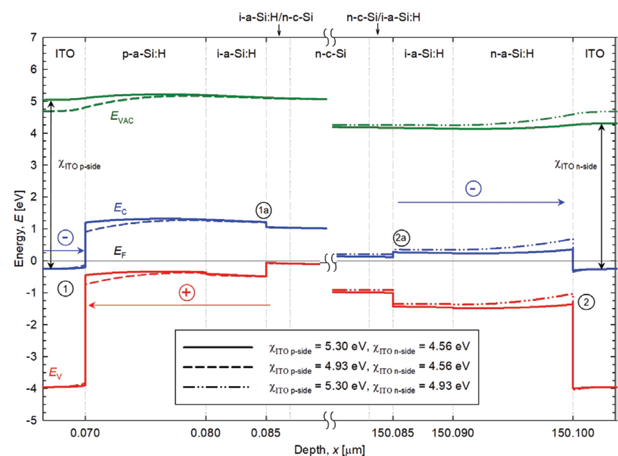

Figure 3: Band-diagrams in thermal equilibrium of the SHJ cell with different electron affinities of ITO layers (χ_{ITO}) at front (p-side) and rear (n-side) of the device (see values in the legend). The reference cell with optimal electron affinities of ITOs is presented by full lines. Symbols E_V, E_F , E_C and E_{VAC} correspond to the conduction-band edge, Fermi level, valence-band edge and the vacuum level, respectively. Circled numbers 1, and 2 mark the ITO/p-a-Si:H and ITO/n-a-Si:H interfaces, respectively. Circled numbers 1a and 2a present the i-a-Si:H/n-c-Si heterojunctions on the p- and n-side of the device, respectively.

In further analysis the $N_{db\text{-}peak}$ parameter of p-a-Si:H and n-a-Si:H layer was chosen for variation since it was pointed out in our previous study that it has detrimental effect on device performance. The variation was done separately for p-a-Si:H and n-a-Si:H layer. In the presented simulation results we varied $N_{db\text{-}peak}$ of both donor and acceptor states (0/- and +/0) simultaneously in a single layer. However, analysis showed that in the case of the p-a-Si:H layer the +/0 type of dangling-bonds affects efficiency the most (see later discussion), whereas the n-a-Si:H layer is affected mostly by the 0/- type.

To illustrate and compare trends related to $N_{db\text{-}peak}$ variation, a series of device simulations were performed where the $N_{db\text{-}peak}$ peak value (height of Gaussian functions) was varied independently of other defect state parameters. Besides the selected reference level of $N_{db\text{-}}$

$_{peak}$ = 1.9e19 cm^{-3}eV^{-1} and 2e19 cm^{-3}eV^{-1} for the p-a-Si:H and n-a-Si:H, respectively, we also included an idealized case with zero $N_{db\text{-}peak}$ (but tail states still present in the material) and the cases with strongly enhanced $N_{db\text{-}peak}$ values up to and including 6e19 cm^{-3}eV^{-1}.

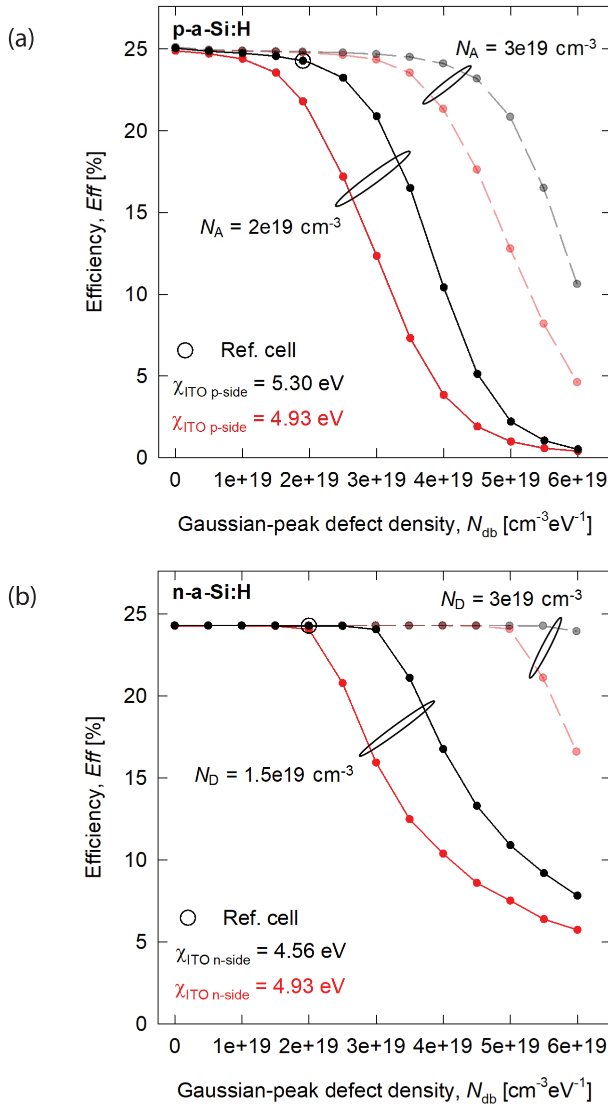

Figure 4: a) Efficiency vs. $N_{db\text{-}peak}$ defect density variation in p-a-Si:H and b) in n-a-Si:H layer. Full lines represent nominal doping concentration of a-Si:H doped layers, whereas the dashed semi-transparent lines represent hypothetical high doping concentration (3e19 cm^{-3}). Cells with optimized values of the adjacent ITO electron affinity are presented by black curves (5.30 eV for the p-side and 4.56 eV for the n-side). Red curves present the non-optimal values (4.93 eV for both p- and n-side of the device). The case for the reference cell (Table 2, Appendix) is circled. It has to be noted that when the electron affinity of ITO is varied on one side of the device, the electron affinity of ITO at the other side is set to the reference (optimized) value.

Besides electron affinities of ITO, two doping levels of p-a-Si:H and n-a-Si:H layers were also included in simulations (reference values and hypothetically high doping values of $N_A = N_D$ = 3e19 cm^{-3} for p- and n-layer respectively). Note that the chosen value for the high levels of doping density presents a purely hypothetical case that cannot be achieved with normal a-Si:H material as they would result in the corresponding activation energy values of ~0.2 eV and ~0.1 eV for the p-a-Si:H and n-a-Si:H layers, which is not achievable in praxis. This hypothetical case is used to indicate the effects related to materials where lower activation energies, and thus, higher effect of doping can be achieved, e.g. nano-crystalline silicon or other meta-materials such as metal oxides. With this hypothetical case we want to stress and quantify the importance of efficient doping of charge carrier selective layers in relation to different ITO contacts.

In Fig. 4a-b the black and red lines present cases with optimal (χ_{ITO} = 5.30 eV and 4.56 eV for the p-a-Si:H and n-a-Si:H layers respectively) and non-optimal electron affinity values of ITO layers (χ_{ITO} = 4.93 eV for both layers), respectively. The hypothetical case of high-doping values is presented with semi-transparent lines. The points on the graphs, presenting the reference case are also encircled.

The results presented in Fig 4a and 4b show that in general the increase of $N_{db\text{-}peak}$ starts to lower the efficiency of the device at all conditions, although the decreases start at different levels of defect states ($N_{db\text{-}peak}$ values).

Focusing first on the p-a-Si:H side of the cell (Fig 4a), in the case with nominal doping level and reference electron affinity of ITO at the p-side (full black line) we can observe that efficiency starts to rapidly drop, when $N_{db\text{-}peak}$ becomes greater than ~2e19 cm^{-3}eV^{-1}. Higher level of doping in this case (dashed semi-transparent black line) shifts this decline of efficiency to $N_{db\text{-}peak}$ values of around 3.5e19 cm^{-3}eV^{-1}. In both cases, reducing the $N_{db\text{-}peak}$ parameter below the reference value will yield an increase in efficiency of less than 1 % when compared to the reference $N_{db\text{-}peak}$. In case of nominal doping we increase the reference efficiency from 24.28 % to ~25 % according to simulations. For higher doping this increase is even less significant. Focusing now on the second case, where the electron affinity of ITO at the p-side is not optimal and doping is nominal (full red line), we can observe that efficiency drops from the reference value of 24.28 % to 21.79 % even at the reference level of the $N_{db\text{-}peak}$ parameter (1.9e19 cm^{-3}eV^{-1}). Additionally, we can see an even faster decline in efficiency as $N_{db\text{-}peak}$ parameter surpasses the 2e19 cm^{-3}eV^{-1} mark. Of note is the observation, that in this case, reducing the $N_{db\text{-}peak}$ significantly below its reference level (1.9e19 cm^{-3}eV^{-1})

mitigates the negative effects of non-optimal electron affinity of ITO. Higher doping (dashed semi-transparent red line) has again a similar effect as before, as it delays the onset and slows down the decline in efficiency until $N_{db\text{-}peak}$ surpasses the 3.5e19 $cm^{-3}eV^{-1}$ mark. Reducing the defect density below 1.9e19 $cm^{-3}eV^{-1}$ does not significantly improve the efficiency also in this case. In general, the negative effects of increasing the defect density are amplified when ITO electron affinity is not optimized (high enough) for the p-a-Si:H layer. The effect can be mitigated by higher doping levels of the pa-Si:H. Additional simulations showed that variation of the ITO band-gap has a much lower effect on efficiency than the electron affinity at different $N_{db\text{-}peak}$ values (not shown here).

The general trends regarding sensitivity of efficiency to the $N_{db\text{-}peak}$ parameter are similar also for the n-a-Si:H layer. Although, it can be observed in the reference case of electron affinities of ITO at the n-side that the efficiency is much less sensitive to defects in the n-a-Si:H layer than that in the p-a-Si:H layer. Further simulation results (not shown in the graphs) revealed that this sensitivity trend remains almost the same when the device is illuminated from either the p- or n-side, and is also independent of the doping type of the c-Si wafer (n- or p-type). Further on, for simulations where non-optimal selection of electron affinities (in this case χ_{ITO} = 4.93 eV) for the ITOs at both p- and n-side of the device (not included in Fig. 4) the sensitivity of the efficiency to variations of $N_{db\text{-}peak}$ in the p-a-Si:H and in the n-a-Si:H layer, surprisingly becomes comparable. It has to be noted that the differences between the reference (close to optimal) and the alternative values of the ITO electron-affinity for both sides are the same but differ in the sign: $\Delta\chi_{ITO}$ = 0.37 eV for the p-side and $\Delta\chi_{ITO}$ = -0.37 eV for the n-side. Additional simulations revealed that using an electron affinity value of 4.36 eV for the ITO at the n-side, which completely mitigates the work function mismatch, does not yield any increase in efficiency because the work function mismatch at the p-side already presents a bottle-neck even when an optimized value of electron affinity (5.3 eV) is used for ITO at the p-side.

A close comparison of the cases where non-optimal electron affinities were applied to ITOs on the p- and n-sides (red lines in Figs. 4a and 4b) and the $N_{db\text{-}peak}$ values were set to their reference values (1.9e19 $cm^{-3}eV^{-1}$ and 2e19 $cm^{-3}eV^{-1}$ for p-a-Si:H and n-a-Si:H respectively) revealed a significant difference between the efficiencies (21.79 % and 24.06 % for the p- and n-side respectively), despite the same work-function mismatch on both sides (ΔWF=0.57 eV). This is due to a difference in the distribution of defect states in p-a-Si:H and n-a-Si:H, with the distribution in p-a-Si:H affecting the cell more severely compared to n-a-Si:H [16]. Additionally, one can observe in Fig. 3, that the conduction band of the ITO and the valence band of p-a-Si:H do not overlap at the heterojunction (encircled 1 in Fig. 3), which means that BBT is not very efficient, thus the transport of charges across the barrier on the p-side is heavily dependent on TAT. On the n-side, however, the transport across the barrier (encircled 2 in Fig. 3) relies on both TAT and Direct tunnelling, which makes the tunnelling on the n-side more efficient compared to the p-side [9], [11], [21] in this case. On a related note, optimal electron affinity of the ITO on the p-side also brings the mentioned energy bands closer together when compared to the non-optimal case (Fig 3.), which not only decreases the work function mismatch, but also improves BBT tunnelling efficiency. The effect is even more pronounced when hypothetically high doping is applied to the p-a-Si:H as activation energy decreases and makes the bands come closer together even more (not shown in Fig. 3). In contrast, on the n-side (encircled 2 in Fig. 3), the lower (optimal) value of the ITO electron affinity separates the conduction band of ITO from the valence band of n-a-Si:H even more, which does not affect the tunnelling noticeably, since BBT is not a factor on this side. However, it does lower the DT barrier height and improves the transport of electrons towards the anode. Similar to the p-side, this effect is even more pronounced when hypothetical levels of doping are applied.

In order to see which tunnelling mechanism is dominant at the ITO/p-a-Si:H and ITO/n-a-Si:H heterointerfaces under various conditions (different electron affinities of ITO and various doping levels of the doped a-Si:H layers), we performed simulations where we applied only one tunnelling mechanism at the time at a specified ITO/a-Si:H heterointerface. The results showed, that TAT is the dominant tunnelling mechanism at the ITO/p-a-Si:H heterointerface for both optimal (5.3 eV) or non-optimal (4.93 eV) values of ITO electron affinity as well as for both realistic (2e19 cm^{-3}) and hypothetical (3e19 cm^{-3}) effective doping density levels of the p-a-Si:H layer. Simulations indicated that the contribution of BBT is negligible compared to TAT in this case. These observations are also in accordance to predictions published in [21]. At the ITO/n-a-Si:H side, however, according to simulation results either TAT or DT on their own can provide a sufficient transport path and yield almost identical efficiencies for both ITO electron affinity values, as well as for both realistic and hypothetically high effective doping levels of the n-a-Si:H layers.

Note, that the change in electron affinity of ITO affects (i) band offsets between the ITO and a-Si:H as well as (ii) the work function mismatch between the materials, that influences the space-charge-region (SCR) prop-

erties of the ITO/a-Si:H heterointerface, which will be discussed later. At the p-a-Si:H side, an increase in electron affinity of ITO also increases band offsets, resulting in higher barriers for electrons and holes (see Fig. 3), which could potentially reduce tunnelling efficiency. However, we observed an increase in efficiency when electron affinity was increased, which means that the possible negative effects of increased band offsets are far outweighed by the positive effects of decreasing the work function mismatch. At the n-side, the reduction of electron affinity results in smaller band offsets as well as a reduction in the work function mismatch and higher efficiency as well. The results indicate, that changes in band offsets due to variation in electron affinity of ITO in the presented range do not significantly affect tunnelling efficiency at the ITO/a-Si:H interface, but the same changes in electron affinity define the work function mismatch, and thus affect the SCR properties of the interface, as will be explained later. Note, that tunnelling must be applied at ITO/a-Si:H heterointerfaces for the cell to function properly, as explained in our previous publication [16]. We would like to state here, that tunnelling is already good enough in both cases of ITO electron affinity on both sides when defect density is not extremely high ($N_{db\text{-}peak}$ < 3e19 cm^{-3}eV^{-1} as efficiency of the cell is above 20 % in those cases. Therefore, the main reasons for the observed efficiency trends when ITO electron affinity is varied and defect density is increased have to be related to other mechanisms.

To further examine and explain the efficiency trends presented in Fig. 4a, we show in Fig. 5a-c also simulation results of the fill-factor (*FF*), short-circuit-current density (J_{SC}) and open-circuit voltage (V_{OC}) of the cell as a function of the $N_{db\text{-}peak}$ parameter in the p-a-Si:H layer. From now on, we will focus on the p-side of the device, recognizing that the defects in the p-a-Si:H layer have a stronger impact on the performance of the device under the given circumstances. Similar to the previous figures, the black and red curves in Fig. 5a-c show cases with optimal χ_{ITO} (5.30 eV on the p-side and 4.56 eV on the n-side), and non-optimal χ_{ITO} values (4.93 eV on both sides). The solid and dashed lines correspond to the nominal (2e19 cm^{-3}) and hypothetically high (3e19 cm^{-3}) doping levels, respectively. The simulation point corresponding to the reference cell (Table 2, Appendix) is circled.

Detailed comparison between the graphs in Fig. 5 reveals that *FF* and V_{OC} are more sensitive to $N_{db\text{-}peak}$, followed by J_{SC}. For the highly doped p-a-Si:H layer one can observe almost no decrease in J_{SC} even for extremely high $N_{db\text{-}peak}$ values, which has to be considered as a hypothetical (idealised) case. These observations also corroborate the statement that tunnelling is sufficient regardless of the chosen ITO electron affinity values. Let us now examine the effects of dangling-bonds in the p-a-Si:H layer on *J*(*V*) curves for some selected cells considering nominal doping levels ($N_{A\ p\text{-}a\text{-}Si:H}$ = 2e19 cm^{-3}) in Fig. 5d. The grey line represents the reference cell (Tables 1, 2) with reference (optimal) electron affinity of ITOs and the reference $N_{db\text{-}peak}$ = 1.9e19 cm^{-3}eV^{-1} in p-a-Si:H. The black curve corresponds to the cell with increased $N_{db\text{-}peak}$ = 2.5e19 cm^{-3}eV^{-1}, the remaining parameters are the same as for the reference cell (Tables 1 and 2). The red curve presents the case with a non-optimal electron affinity of ITO ($\chi_{ITO\ p\text{-}a\text{-}Si:H}$ = 4.93 eV) and increased $N_{db\text{-}peak}$. The selected curves reflect the trends observed for the related parameters (J_{SC}, V_{OC}, *FF*) in the region of moderate increase in $N_{db\text{-}peak}$. J(V) curves indicate that besides lower V_{OC}, the *FF* decreased mostly due to the drop of the voltage at the maximum power point (V_{MPP}) as indicated in the figure. The same general trend is observed for all cells, with different electron affinity of ITO layers, however the scale of change is different. The drop in V_{MPP} is more pronounced when non-optimal electron affinity of ITO is used, and even more-so when defect states are increased. Of note is also the observation that applying non-optimal electron affinity of ITO alone decreases the *FF* in a similar manner as increasing only the defect states since V_{MPP} drops in both cases.

We found that the explanation for the decrease of V_{MPP} and V_{OC} can be related to the Poisson equation and how the total charge (free holes and electrons, ionized dopants and trapped charge) determines the final voltage of the cell when electron affinity of ITO and dangling-bond defect states are varied. In our previous publication [16] we explained in great detail how the voltage drops due to increased defect density and related charge re-distribution as the electric field that is needed for charge separation becomes weaker. We also explained that work-function mismatch dictates the amount of ionized ITO charge that needs to be screened in the adjacent a-Si:H layer in order to obtain a sufficient electric field in the c-Si bulk that is needed for charge separation and good MPP voltages [16]. When ITO with a non-optimal electron affinity is applied, as was the case here, the work function mismatch is increased. Then, higher dangling-bond defect density reduces the charge-screening capability of the p-a-Si:H which leads to an even lower electric field and the observed trends of low V_{MPP} and V_{OC}.

Changes in electron affinity of ITO directly affect the ITO work function. When the work function of ITO is smaller than that of p-a-Si:H (the difference is referred to as work function mismatch), electrons (mediated by tunnelling) flow from ITO toward p-a-Si:H and a positively charged part of the space-charge-region (SCR) is

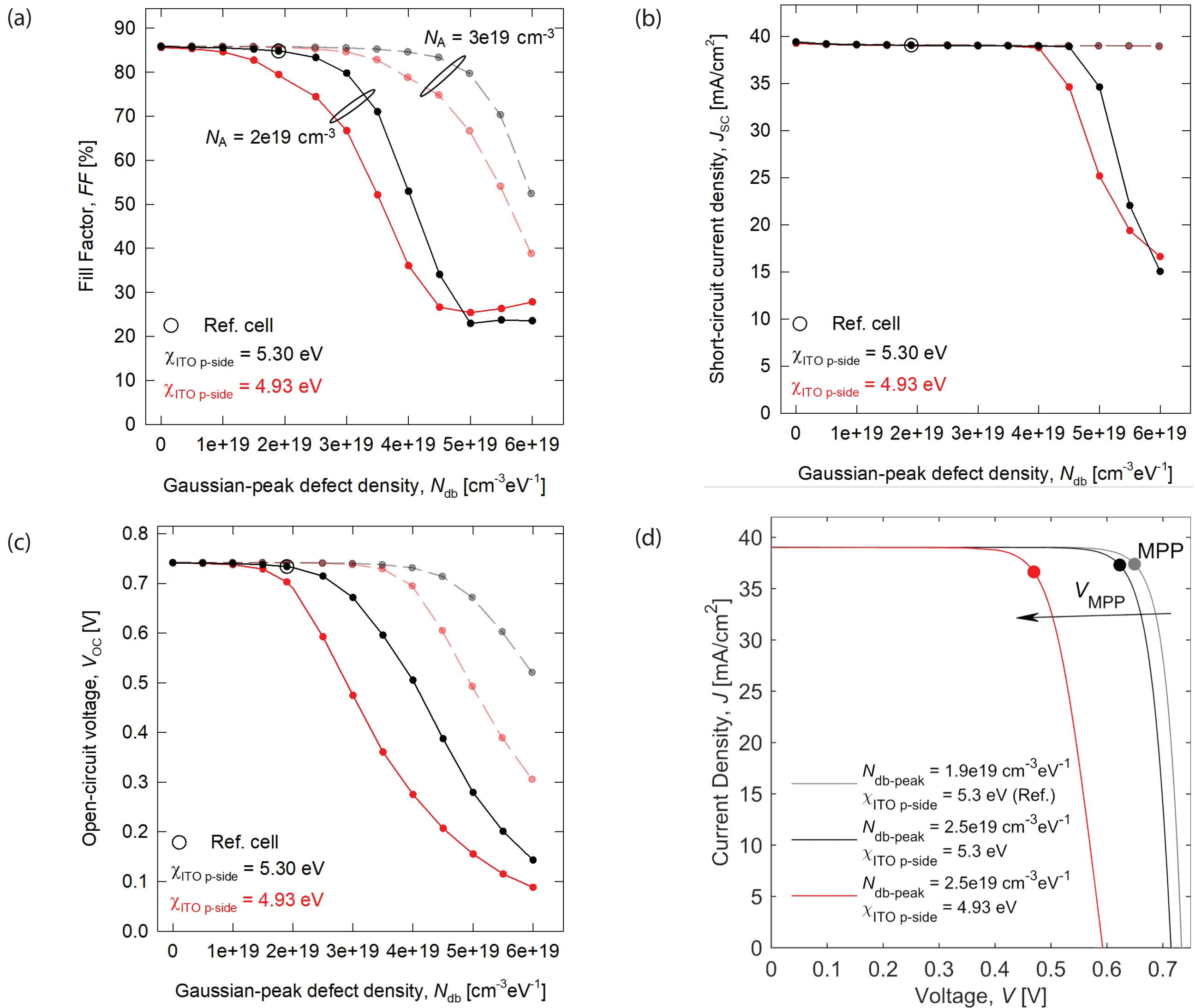

Figure 5: a) *FF*, b) V_{OC}, c) J_{SC} vs. $N_{db\text{-}peak}$ defect-density variation in the p-a-Si:H layer. Full lines correspond to nominal doping density of p-a-Si:H layer (2e19 cm^{-3}), whereas dashed lines represent the device with high doping density $N_{A\ p\text{-}a\text{-}Si:H}$ = 3e19 cm^{-3}). Devices with reference (optimal) values of the ITO electron affinities are presented by black curves (χ_{ITO} = 5.3 eV for the p-side and 4.56 eV for the ITO at the n-side). Red curves correspond to cases where ITOs are not optimal (χ_{ITO} = 4.93 eV for both p- and n-side of the device). The legend in a) applies also to b) and c). d) $J(V)$ curve for the reference cell (grey) and selected cases with high $N_{db\text{-}peak}$ (2.5e19 cm^{-3}eV^{-1}) and ITO electron affinity at the p-side set to 5.30 eV (black) and 4.93 eV (red). All presented cases were simulated at nominal doping level of the p-a-Si:H layer (2e19 cm^3).

formed on the ITO side of the ITO/p-a-Si:H heterojunction (due to ionized donor atoms), whereas the negatively charged part of the SCR forms in the p-a-Si:H due to ionized acceptor dopants and neutralized +/0 states (that are now occupied by electrons that came from ITO and no longer contribute to the positive charge). The resulting electric field is oriented in the opposite direction than the electric field at the i-a-Si:H/n-c-Si heterojunction. As the work function mismatch is increased, the SCR is broadened even deeper into the p-a-Si:H region. The broadening of this SCR is actually depleting the p-a-Si:H layer, which can result in a weaker electric field (needed for charge separation) in the n-c-Si absorber when the SCR is not well contained in the p-a-Si:H. The mentioned changes affect the redistribution of charges throughout the device, which also determines the external voltage.

In order to mitigate the negative effect of the work function mismatch, that lowers the voltage (V_{MPP} and V_{OC}) and *FF*, at the ITO/p-a-Si:H (n-a-Si:H) heterointerface, the negative (positive) charge in the p-a-Si:H (n-a-Si:H) layer must be able to screen the opposite charge in the SCR of ITO. The screening capability of a-Si:H de-

pends on effective doping concentration, defect density and layer thickness. Thicker layers with high doping concentrations and low defect density are capable of screening more ITO charge. The increase in dangling-bond defect density mitigates the positive effect of doping and reduces the screening capability of the layer. In addition, as we discussed in our previous publication [16], an increase in peak dangling-bond defect density ($N_{db\text{-}peak}$) in the p-a-Si:H layer reduced both V_{OC} and *FF*, whereas J_{SC} changed only slightly. The drop in *FF* was explained by lowering of the V_{MPP}, whereas J_{MPP} was observed to be almost unaffected, since at MPP conditions, total recombination was still far smaller compared to optically generated current. We concluded, that an increase in $N_{db,\ peak}$ reduces efficiency especially due to lower V_{MPP} ($Eff = \frac{J_{SC} \cdot V_{OC} \cdot FF}{P_{in}} = \frac{J_{MPP} \cdot V_{MPP}}{P_{in}}$).

To explain the drop in V_{MPP} we followed the Poisson's equation, which relates charge distribution to the voltage between the terminals. A thorough analysis of total charge and all of its components (free charge, trapped charge in defect states and ionized dopant atoms) revealed that the increase in $N_{db\text{-}peak}$ in p-a-Si:H resulted in a reduction of positive charge in the SCR of ITO and a reduction of negative charge in the SCR of p-a-Si:H. The reduction of negative charge in p-a-Si:H was shown to be an increase in positive charge in the p-a-Si:H layer due to unoccupied +/0 dangling-bond states, that are positioned at energies where they are unlikely to be occupied by an electron and remained positively charged. We used the Poisson's equation and showed, that this virtual shift of positive charge from ITO into the p-a-Si:H layer due to an increase in $N_{db\text{-}peak}$ resulted in the observed reduction in V_{MPP}. We also showed, that 0/- states remained neutral and did not significantly affect the total charge in p-a-Si:H. All of the above is true also for all the cases presented in this work (both doping levels and dangling-bond defect densities).

Before moving on to conclusions, we would like to provide a brief commentary regarding the reference efficiency of our simulated device (24.28 %), where both ITO layers have optimal electron affinity values (5.3 eV and 4.56 eV for the p- and n-side, respectively). It has been reported that SHJ cells have the potential to reach efficiencies as high as ~27 % [9]. However, this can be achieved by employing additional layers, such as p-type SiC_x or SiO_x and using the IBC architecture. Without these additional layers, the record cell, made by Kaneka, reached efficiency of 26.7 % [42], thanks to the IBC design, that allows for high J_{SC} = 42.65 mA/cm^2. In comparison, our reference cell, that uses optimized ITO layers, achieves J_{SC} = 39.02 mA/cm^2. Should we calculate the efficiency of our reference cell, by using the J_{SC} of the record cell, we would get efficiency around 26.5 %, which is also in accordance to the simulations presented in other publications that were simulating and optimizing IBC SHJ solar cells [9]. Therefore, the difference between the efficiencies of IBC and planar architectures can be mostly attributed to better J_{SC} of IBC devices. In addition, the V_{OC} and *FF* values of our reference cell simulations are very similar to the ones reported for the record cell and comparable to the ones presented in [9].

4 Conclusion

We applied opto-electrical modelling of a SHJ solar cell to study ITO/doped a-Si:H selective contacts in terms of ITO electron affinity and dangling-bond Gaussian peaks (amphoteric defects) of the doped a-Si:H layers. In the simulation structure, the ITO layer at the p- and n-side of the device was considered as a full semiconductor layer. DT, BBT and TAT tunnelling mechanisms were included in simulations at ITO/doped a-Si:H selective contacts. We demonstrated that optimizing the electron affinity of the ITO layers is critical when the doped a-Si:H layers are insufficiently doped or have high concentrations of dangling-bond defect states. We showed that optimization of electron affinity of ITO is especially important at the p-side of the device due to a less favourable trap distribution and poorer tunnelling efficiency compared to the n-side. We showed that the ITO at the p-a-Si:H layer should have electron affinity as high as possible (~5.3 eV) in order to minimize the work function mismatch (which was only 0.2 eV in this case), as higher values of the work function mismatch can deplete the p-a-Si:H layer to the point, where it is unable to sufficiently screen the positive charge in the space-charge-region of ITO, resulting in a diminished electric field in the n-c-Si absorber, and consequently poor charge separation capability of the cell, leading to a reduction in *FF* and V_{OC}. Conversely, the ITO at the n-a-Si:H layer should have electron affinity as low as 4.56 eV (work function mismatch is 0.2 eV in this case). Lower values of electron affinity enabling lower work function mismatch on the n-side did not further improve efficiency, due to the already present work function mismatch at the p-side (0.2 eV in the optimal case). Low values of V_{OC} also confirmed poor charge-separation capability of the cell, when electron affinity of ITO results in a higher work function mismatch between the ITOs and doped a-Si:H layers. We demonstrated that the work function mismatch between ITO and doped a-Si:H layers makes the solar cell efficiency more sensitive to increased dangling-bond defect states in the doped a-Si:H layers as higher dangling-bond defect density reduces the layers' ability to screen the charge in the SCR of ITO as it negates the positive effect of doping. We also observed that when

ITO electron affinity at the p-a-Si:H (n-a-Si:H) layer is lower than 5.3 eV (higher than 4.56 eV) and doping is nominal (2e19 cm^{-3} and 1.5e19 cm^{-3} for p-a-Si:H and n-a-Si:H, respectively), only the *FF* (and not V_{OC} or J_{SC}) can be improved by lowering the dangling-bond defect density below the reference level (1e19 $cm^{-3}eV^{-1}$). In contrast, J_{SC} was affected only at extremely high levels of defect densities even when electron affinity of ITO at the p-a-Si:H (n-a-Si:H) was lower (higher) than 5.3 eV (4.56 eV). We also concluded that tunnelling efficiency at the ITO/a-Si:H interface is not significantly affected by the changes in the band offsets, caused by variation in electron affinity of ITO, whereas the changes in the work function mismatch, as the SCR properties of the heterointerface were changed, affected the cell significantly. An increase in electron affinity of ITO at the p-a-Si:H layer results in increased conduction and valence band offsets, but the reduction in work function mismatch outweighs the negative impact of increased barrier heights and an increase in efficiency was observed, whereas a reduction in electron affinity of ITO at the n-a-Si:H layer results in even lower band offsets as well as a reduction in work function mismatch. It was also shown that TAT is the dominant transport mechanism at the ITO/p-a-Si:H heterojunction for all presented cases. At the ITO/n-a-Si:H interface, both DT and TAT provide an efficient transport path and yield very similar results when either of the two is applied as the only tunnelling mechanism at that interface. Results presented in this paper give indications for acceptable defect levels in doped amorphous-silicon layers in relation to optimality of ITO electron affinity for the ITO/a-Si:H selective contacts and can serve as a roadmap when designing selective contacts with alternative materials for SHJ cells.

5 Appendix

Table 2: Input parameters for the reference case

Quantity	Symbol	n-c-Si	p-a-Si:H	n-a-Si:H	i-a-Si:H	i-a-Si:H/n-c-Si	ITO
Relative Dielectric Constant	ε_r	11.9 [43]	11.9 [43]	11.9 [43]	11.9 [43]	11.9 [43]	8.9 [44]
Electron Affinity	χ (eV)	4.05 [12]	3.9 [12]	3.9 [12]	3.9 [12]	4.05 [12]	5.3 / 4.56 (p-side/n-side) [40]
Band-gap (Mobility-gap)	E_{gap} (eV)	1.12 [36]	1.65 [12]	1.72 [12]	1.70 [12]	1.12 [36]	3.7 [9]
Effective Doping Conc.	N_D / N_A (cm^{-3})	2e+15 / 0 [12]	0 / 2e+19 [12]	1.5e+19 / 0 [12] *	2.2e+15 / 0 [12]	2e+15 / 0 [12]	1e+20 / 0 [9]
Density of States	N_C / N_V (cm^{-3})	2.8e+19 / 3.1e+19 [43]	2e+20 / 2e+20 [43]	2e+20 / 2e+20 [43]	2e+20 / 2e+20 [43]	2.8e+19 / 3.1e+19 [43]	4.12e+18 / 1.17e+19 [44], [45]
SRH life-times	τ_e / τ_h (ms)	1 / 10 [36]	/	/	/	1/10 [36]	/
Mobilities	μ_e / μ_h (cm^2/Vs)	1342 / 452 [43]	10 / 1 [12]	10 / 1 [12]	10 / 1 [12]	1342 / 452 [43]	50 / 30 [9]
Tunnelling mass (DT, TAT and BBT)	m*	/	0.1 [9]	0.1 [9]	0.1 [9]	0.1 [9]	0.1 [9]
Trap volume (TAT)	V_{trap} (μm^{-3})	/	1e-11 [8]	1e-11 [8]	1e-11 [8]	1e-11 [8]	/
Huang-Rhys con. (TAT)	H_{rhys}	/	2 [8]	2 [8]	2 [8]	2 [8]	/
Phonon Energy (TAT)	E_{ph} (meV)	/	37.78 [8]	37.78 [8]	37.78 [8]	37.78 [8]	/
Coupling factor (DIRECT, BBT)	g_e/g_h	/	1 / 1 [9]	1 / 1 [9]	1 / 1 [9]	1 / 1 [9]	1 / 1 [9]

* Effective doping concentration was changed from the reference to obtain realistic activation energy for the n-a-Si:H layer (200 meV)

6 Acknowledgments

The authors acknowledge the financial support from the Slovenian Research Agency-ARRS (program P2-0415 and PhD funding for J.B.).

7 References

1. F. ISE, 'Photovoltaics Report', 2020. [Online]. Available: https://www.ise.fraunhofer.de/content/dam/ise/de/documents/publications/studies/Photovoltaics-Report.pdf
2. M. A. Green, E. D. Dunlop, J. Hohl-Ebinger, M. Yoshita, N. Kopidakis, and X. Hao, 'Solar cell efficiency tables (version 56)', *Progress in Photovoltaics: Research and Applications*, vol. 28, no. 7, pp. 629–638, 2020, https://doi.org/10.1002/pip.3303.
3. K. Yoshikawa *et al.*, 'Silicon heterojunction solar cell with interdigitated back contacts for a photoconversion efficiency over 26%', *Nature Energy*, vol. 2, p. 17032, Mar. 2017.
4. A. Richter, M. Hermle, and S. W. Glunz, 'Reassessment of the Limiting Efficiency for Crystalline Silicon Solar Cells', *IEEE Journal of Photovoltaics*, vol. 3, no. 4, pp. 1184–1191, Oct. 2013, https://doi.org/10.1109/JPHOTOV.2013.2270351.
5. H. Bashiri, M. A. Karami, and S. M. Nejad, 'Heterojunction silicon solar cells performance optimization and sensitivity reduction to the interface defect states', *Mater. Res. Express*, vol. 4, no. 12, p. 126308, Dec. 2017, https://doi.org/10.1088/2053-1591/aa9c91.
6. M. Filipič, Z. C. Holman, F. Smole, S. D. Wolf, C. Ballif, and M. Topič, 'Analysis of lateral transport through the inversion layer in amorphous silicon/crystalline silicon heterojunction solar cells', *J Appl Phys*, vol. 114, no. 7, p. 074504, Aug. 2013, https://doi.org/10.1063/1.4818709.
7. A. Kanevce and W. K. Metzger, 'The role of amorphous silicon and tunneling in heterojunction with intrinsic thin layer (HIT) solar cells', *Journal of Applied Physics*, vol. 105, no. 9, pp. 094507–1, May 2009, https://doi.org/10.1063/1.3106642.
8. C. Messmer, M. Bivour, C. Luderer, L. Tutsch, J. Schon, and M. Hermle, 'Influence of Interfacial Oxides at TCO/Doped Si Thin Film Contacts on the Charge Carrier Transport of Passivating Contacts', *IEEE J. Photovoltaics*, vol. 10, no. 2, pp. 343–350, Mar. 2020, https://doi.org/10.1109/JPHOTOV.2019.2957672.
9. P. Procel, G. Yang, O. Isabella, and M. Zeman, 'Theoretical evaluation of contact stack for high efficiency IBC-SHJ solar cells', *Solar Energy Materials and Solar Cells*, vol. 186, pp. 66–77, Nov. 2018, https://doi.org/10.1016/j.solmat.2018.06.021.
10. P. Procel *et al.*, 'Opto-electrical modelling and optimization study of a novel IBC c-Si solar cell', *Progress in Photovoltaics: Research and Applications*, vol. 25, no. 6, pp. 452–469, Jun. 2017, https://doi.org/10.1002/pip.2874.
11. P. Procel *et al.*, 'On the correlation between contact resistivity and high efficiency in (IBC-) SHJ solar cells', *36th European Photovoltaic Solar Energy Conference and Exhibition*, pp. 251–254, 2019.
12. Z. Shu, U. Das, J. Allen, R. Birkmire, and S. Hegedus, 'Experimental and simulated analysis of front versus all-back-contact silicon heterojunction solar cells: effect of interface and doped a-Si:H layer defects', *Prog. Photovolt: Res. Appl.*, vol. 23, no. 1, pp. 78–93, Jan. 2015, https://doi.org/10.1002/pip.2400.
13. R. Varache, J. P. Kleider, M. E. Gueunier-Farret, and L. Korte, 'Silicon heterojunction solar cells: Optimization of emitter and contact properties from analytical calculation and numerical simulation', *Materials Science and Engineering: B*, vol. 178, no. 9, pp. 593–598, May 2013, https://doi.org/10.1016/j.mseb.2012.11.011.
14. M. Vukadinović, F. Smole, M. Topič, R. E. I. Schropp, and F. A. Rubinelli, 'Transport in tunneling recombination junctions: A combined computer simulation study', *Journal of Applied Physics*, vol. 96, no. 12, pp. 7289–7299, Dec. 2004, https://doi.org/10.1063/1.1811375.
15. Synopsys, 'Sentaurus™ Device User Guide: Release Q-2019.12'. 2019. [Online]. Available: http://www.synopsys.com
16. J. Balent, F. Smole, M. Topic, and J. Krc, 'Numerical Analysis of Selective ITO/a-Si:H Contacts in Heterojunction Silicon Solar Cells: Effect of Defect States in Doped a-Si:H Layers on Performance Parameters', *IEEE J. Photovoltaics*, pp. 1–14, 2021, https://doi.org/10.1109/JPHOTOV.2021.3063019.
17. M. Bivour, S. Schröer, and M. Hermle, 'Numerical Analysis of Electrical TCO / a-Si:H(p) Contact Properties for Silicon Heterojunction Solar Cells', *Energy Procedia*, vol. 38, pp. 658–669, Dec. 2013, https://doi.org/10.1016/j.egypro.2013.07.330.
18. S. Kirner *et al.*, 'The Influence of ITO Dopant Density on J-V Characteristics of Silicon Heterojunction Solar Cells: Experiments and Simulations', *Energy Procedia*, vol. 77, pp. 725–732, Aug. 2015, https://doi.org/10.1016/j.egypro.2015.07.103.
19. M. Mikolášek, 'Silicon Heterojunction Solar Cells: The Key Role of Heterointerfaces and their Impact on the Performance', in *Nanostructured Solar Cells*, N. Das, Ed. InTech, 2017. https://doi.org/10.5772/65020.

20. L. Zhao, C. L. Zhou, H. L. Li, H. W. Diao, and W. J. Wang, 'Role of the work function of transparent conductive oxide on the performance of amorphous/crystalline silicon heterojunction solar cells studied by computer simulation', *phys. stat. sol. (a)*, vol. 205, no. 5, pp. 1215–1221, May 2008, https://doi.org/0.1002/pssa.200723276.
21. P. Procel *et al.*, 'The role of heterointerfaces and subgap energy states on transport mechanisms in silicon heterojunction solar cells', *Progress in Photovoltaics: Research and Applications*, vol. 28, no. 9, pp. 935–945, Sep. 2020, https://doi.org/0.1002/pip.3300.
22. J. Bullock *et al.*, 'Efficient silicon solar cells with dopant-free asymmetric heterocontacts', *Nature Energy*, vol. 1, no. 3, p. 15031, Jan. 2016, https://doi.org/10.1038/nenergy.2015.31.
23. R. Islam, P. Ramesh, Ju Hyung Nam, and K. C. Saraswat, 'Nickel oxide carrier selective contacts for silicon solar cells', Jun. 2015, pp. 1–4. https://doi.org/10.1109/PVSC.2015.7355921.
24. M. Mews, A. Lemaire, and L. Korte, 'Sputtered Tungsten Oxide as Hole Contact for Silicon Heterojunction Solar Cells', *IEEE Journal of Photovoltaics*, vol. 7, no. 5, pp. 1209–1215, Sep. 2017, https://doi.org/10.1109/JPHOTOV.2017.2714193.
25. D. Sacchetto *et al.*, 'ITO/MoOx/a-Si:H(i) Hole-Selective Contacts for Silicon Heterojunction Solar Cells: Degradation Mechanisms and Cell Integration', *IEEE Journal of Photovoltaics*, vol. 7, no. 6, pp. 1584–1590, Nov. 2017, https://doi.org/10.1109/JPHOTOV.2017.2756066.
26. Y. Wan *et al.*, 'Magnesium Fluoride Electron-Selective Contacts for Crystalline Silicon Solar Cells', *ACS Applied Materials & Interfaces*, vol. 8, no. 23, pp. 14671–14677, Jun. 2016, https://doi.org/10.1021/acsami.6b03599.
27. W. Yoon *et al.*, 'Hole-selective molybdenum oxide as a full-area rear contact to crystalline p-type Si solar cells', *Japanese Journal of Applied Physics*, vol. 56, no. 8S2, p. 08MB18, Aug. 2017, https://doi.org/10.7567/JJAP.56.08MB18.
28. J. Krč, S. Franc, and T. Marko, 'One-dimensional semi-coherent optical model for thin film solar cells with rough interfaces', in *Informacije MIDEM 32*, Ljubljana, 2002, vol. 2002.
29. Z. Lokar *et al.*, 'Coupled modelling approach for optimization of bifacial silicon heterojunction solar cells with multi-scale interface textures', *Optics Express*, vol. 27, no. 20, p. A1554, Sep. 2019, https://doi.org/10.1364/OE.27.0A1554.
30. A. Richter, S. W. Glunz, F. Werner, J. Schmidt, and A. Cuevas, 'Improved quantitative description of Auger recombination in crystalline silicon', *Phys. Rev. B*, vol. 86, no. 16, p. 165202, Oct. 2012, https://doi.org/10.1103/PhysRevB.86.165202.
31. S. Olibet, E. Vallat, and C. Ballif, 'Model for a-Si:H/C-Si interface recombination based on the amphoteric nature of silicon dangling bonds', *Physical Review B*, vol. 76, Jul. 2007, https://doi.org/10.1103/PhysRevB.76.035326.
32. D. Schroeder, *Modelling of Interface Carrier Transport for Device Simulation*. Vienna: Springer Vienna, 1994. https://doi.org/10.1007/978-3-7091-6644-4.
33. K. Horio and H. Yanai, 'Numerical modeling of heterojunctions including the thermionic emission mechanism at the heterojunction interface', *IEEE Trans. Electron Devices*, vol. 37, no. 4, pp. 1093–1098, Apr. 1990, https://doi.org/10.1109/16.52447.
34. F. Jiménez-Molinos, F. Gámiz, A. Palma, P. Cartujo, and J. A. López-Villanueva, 'Direct and trap-assisted elastic tunneling through ultrathin gate oxides', *Journal of Applied Physics*, vol. 91, no. 8, pp. 5116–5124, Apr. 2002, https://doi.org/10.1063/1.1461062.
35. A. Palma, A. Godoy, J. A. Jiménez-Tejada, J. E. Carceller, and J. A. López-Villanueva, 'Quantum two-dimensional calculation of time constants of random telegraph signals in metal-oxide–semiconductor structures', *Phys. Rev. B*, vol. 56, no. 15, pp. 9565–9574, Oct. 1997, https://doi.org/10.1103/PhysRevB.56.9565.
36. A. Fell *et al.*, 'Input Parameters for the Simulation of Silicon Solar Cells in 2014', *IEEE Journal of Photovoltaics*, vol. 5, no. 4, pp. 1250–1263, Jul. 2015, https://doi.org/10.1109/JPHOTOV.2015.2430016.
37. M. Baudrit and C. Algora, 'Tunnel Diode Modeling, Including Nonlocal Trap-Assisted Tunneling: A Focus on III–V Multijunction Solar Cell Simulation', *IEEE Transactions on Electron Devices*, vol. 57, no. 10, pp. 2564–2571, Oct. 2010, https://doi.org/10.1109/TED.2010.2061771.
38. MeiKei Ieong, P. M. Solomon, S. E. Laux, H.-S. P. Wong, and D. Chidambarrao, 'Comparison of raised and Schottky source/drain MOSFETs using a novel tunneling contact model', in *International Electron Devices Meeting 1998. Technical Digest (Cat. No.98CH36217)*, San Francisco, CA, USA, 1998, pp. 733–736. https://doi.org/10.1109/IEDM.1998.746461.
39. E. O. Kane, 'Theory of Tunneling', *Journal of Applied Physics*, vol. 32, no. 1, pp. 83–91, Jan. 1961, https://doi.org/10.1063/1.1735965.
40. A. Klein *et al.*, 'Transparent Conducting Oxides for Photovoltaics: Manipulation of Fermi Level, Work Function and Energy Band Alignment', *Materials*, vol. 3, no. 11, pp. 4892–4914, Nov. 2010, https://doi.org/10.3390/ma3114892.
41. E. Fortunato, D. Ginley, H. Hosono, and D. C. Paine, 'Transparent Conducting Oxides for Photovol-

taics', *MRS Bull.*, vol. 32, no. 3, pp. 242–247, Mar. 2007,
https://doi.org/10.1557/mrs2007.29.

42. M. A. Green, E. D. Dunlop, J. Hohl-Ebinger, M. Yoshita, N. Kopidakis, and A. W. Y. Ho-Baillie, 'Solar cell efficiency tables (Version 55)', *Progress in Photovoltaics: Research and Applications*, vol. 28, no. 1, pp. 3–15, Jan. 2020,
https://doi.org/10.1002/pip.3228.
43. M. Filipic, F. Smole, and M. Topic, 'Optimization of interdigitated back contact geometry in silicon heterojunction solar cell', in *Numerical Simulation of Optoelectronic Devices, 2014*, Palma de Mallorca, Sep. 2014, pp. 161–162.
https://doi.org/10.1109/NUSOD.2014.6935406.
44. L. Gupta, A. Mansingh, and P. K. Srivastava, 'Band gap narrowing and the band structure of tin-doped indium oxide films', *Thin Solid Films*, vol. 176, no. 1, pp. 33–44, Sep. 1989,
https://doi.org/10.1016/0040-6090(89)90361-1.
45. F. Fuchs and F. Bechstedt, 'Indium-oxide polymorphs from first principles: Quasiparticle electronic states', *Phys. Rev. B*, vol. 77, no. 15, p. 155107, Apr. 2008,
https://doi.org/10.1103/PhysRevB.77.155107.

Copyright © 2022 by the Authors. This is an open access article distributed under the Creative Commons Attribution (CC BY) License (https://creativecommons.org/licenses/by/4.0/), which permits unrestricted use, distribution, and reproduction in any medium, provided the original work is properly cited.

Arrived: 11. 03. 2022
Accepted: 08. 07. 2022